

This manuscript has been submitted for publication in MARINE AND PETROLEUM GEOLOGY. Please note that the manuscript has not yet undergone peer-review. Subsequent versions of this manuscript may have slightly different content. If accepted, the final version of this manuscript will be available via the 'Peer-reviewed Publication DOI' link on the right-hand side of this webpage.

1 Forced folding and fracturing induced by differential compaction
2 during post-depositional inflation of sandbodies: insights from
3 numerical modelling

4 Qingfeng Meng*, David Hodgetts

5 *1. School of Earth and Environmental Sciences, University of Manchester, Manchester, M13 9PL,*
6 *UK*

7 **Abstract**

8 Three series of numerical models based on the discrete element method were constructed to
9 simulate forced folding and fracturing triggered by postdepositional inflation of fluidised sandbody.
10 The models consist of numerous particles that have relatively low to high interparticle bonds to
11 represent overburden sediments with a relatively low to high cohesion, and cohesionless,
12 frictionless particles to represent fluidised sands. The modelling results show that normal faults
13 were produced due to the upward inflation of sand domes and the resulting flexed overburden,
14 when the cohesion of the host sediments is low. Opening voids were created as a result of strata
15 collapse, when the intrusion-related normal faults terminated within the host sediments as blind
16 faults. Conical fractures that are aligned along sandbody margins were produced, which consist of
17 closed, lower segments with a reverse displacement, and opening, middle-upper segments with a
18 minor to zero shear component. Forced folds were generated in most models with a moderate to
19 high cohesion, resulting in differential compaction in the overlying sediments that can account for
20 the formation of fold-related fractures, which are either shear, hybrid or pure tensile, depending
21 on their structural positions. The amplitude of forced folds is closely associated with both cohesion

* Corresponding author. E-mail address: meng.qingfeng@hotmail.com

22 and thickness of sediments in the overburden, whilst fold wavelength is mainly controlled by
23 sediment cohesion. Based on the modelling results, three types of preferential sites for the storage
24 of injected sands were suggested, which are believed to be instructive for subsurface sandbody
25 detection and prediction. This study demonstrates that differential compaction induced by sand
26 inflation can play an important role in overburden folding and fracturing.

27

28 **Key words:** forced fold; fracture; sandbody; sandstone intrusion; numerical modelling; discrete
29 element

30

31 **1. Introduction**

32 Sandstone intrusions have been extensively studied with a long history of field-based research
33 focused on meter-scale intrusive bodies (e.g. Diller, 1890; Jenkins, 1930; Peterson, 1966; Boehm
34 and Moore, 2002; Huuse et al., 2005a; Hubbard et al., 2007; Vétel and Cartwright, 2010; Hurst et
35 al., 2011; Moreau et al., 2012; Scott et al., 2013; Palladino et al., 2016, 2018; among many others).
36 The study on large-scale sandstone intrusions has become increasing common in the past two
37 decades using high-resolution three-dimensional seismic data from basins where such structures
38 are developed (e.g. Molyneux et al., 2002; Hurst et al., 2003a; Hurst et al., 2003b; Cartwright and
39 Huuse, 2005; Davies et al., 2006; Cartwright, 2007; Cartwright et al., 2007; Huuse et al., 2005b,
40 2007, 2010; Lonergan et al., 2007; Vigorito et al., 2008; Jackson et al., 2011). Understanding the
41 mechanisms of sandstone intrusions is critically important, not only because that they can
42 significant influence reservoir architecture (Fig. 1) and connectivity, reservoir volumetrics and
43 pore-scale reservoir properties (Lonergan et al., 2000) and thereby affect hydrocarbon exploration
44 and production from those reservoirs (Huuse et al., 2003; de Boer et al., 2007; Hurst and Cartwright,

45 2007; Hurst et al., 2006, 2007, 2016; Hurst and Vigorito, 2017), but also because of their crucial
46 role in understanding petroleum systems and basin evolution in general (Cartwright, 2010).

47

48 The geometric variability and distribution of subsurface sandstone intrusions can be extremely
49 complex and be difficult to map because they are commonly at or below seismic resolution
50 (Jackson et al., 2007). Many researchers have attempted to develop conceptual models of sand-
51 intrusion processes and the associated deformations in the overburden, shedding light on channel
52 surface geometries (Lonergan et al., 2000), development of forced folds (Cosgrove and Hillier,
53 1999; Shoulders and Cartwright, 2004; Frey-Martinez et al., 2007; Szarawarska et al., 2010),
54 formation and propagation of intrusion-related faults/fractures in the overlying sediments
55 (Rodrigues et al., 2009; Mourgues et al., 2012; Bureau et al., 2014; Haug et al., 2018), and
56 interactions of sand intrusions with pre-existing structures (Lonergan and Cartwright, 1999;
57 Molyneux et al., 2002; Shoulders et al., 2007; Bureau et al., 2013; Løseth et al., 2013). In particular,
58 sandstone intrusions that occur in a conical form (Molyneux et al., 2002; Huuse et al., 2005a;
59 Jackson et al., 2007; Shoulders et al., 2007; Cartwright et al., 2008; Jackson et al., 2011), or
60 referred to as wings (Huuse et al., 2004), have received great attention, however, their formation
61 mechanics still remains controversial. Although sandstone intrusions have been more commonly
62 suggested as hydraulic fractures, it has been realized that differential compaction induced by
63 sandbody inflation may have played an important role in the formation of some dykes and sills,
64 especially some peripheral dykes (Cosgrove and Hillier, 2000; Huuse et al., 2004). This is often
65 evident from the domal or irregular sandbody surfaces and the flexed overburden (Lonergan et al.,
66 2000; Frey-Martinez et al., 2007; Cartwright et al., 2008; Jackson et al., 2011) or the 'jack-up'
67 phenomenon (Szarawarska et al., 2010).

68

69 This paper reports the modelling results of overburden deformation induced by inflation of fluidised
70 sandbody using the discrete element method. The aims of this paper are (1) to produce various
71 types of structures that are associated with sandstone inflation and are comparable to those
72 observed in nature; (2) to investigate the role of sediment cohesion and thickness in the
73 development of forced fold; and (3) to better understand the formation mechanisms of dyke-sill
74 complexes associated with postdepositional sandbody activities, especially those occurring in a
75 mixed shear-extensional mode. The models presented provide new insights into the development
76 and controls on forced folding and fracturing during sandstone inflation, and are believed to be
77 applicable for the detection and prediction of subsurface sandstone injectites.

78

79 **2. Methodology**

80 **2.1. Fundamental principles**

81 The discrete element modelling method, based on elastic interactions between frictional rigid
82 particles, was first developed by Cundall and Strack (1979) to simulate behavior and interaction
83 of granular materials. The modelled materials consist of numerous elastic particles that displace
84 independently from one another, and interact with neighbouring particles only at contacts between
85 particles. Particle contact is defined as a linear spring in compression that resist particle overlap,
86 and a frictional strength that resists shear motion (Fig. 2a). More complex behavior of a particle
87 assembly can be simulated by allowing the particles to be bonded together so as to resist both shear
88 and extensional displacements. The bonds will be broken once the bond strength is exceeded,
89 which indicates the generation of microfractures. Coalescence of microfractures can subsequently
90 result in larger macro sized fractures.

91

92 The mechanical behavior of a particle assembly is characterised by the movement of each particle
93 and inter-particle forces acting on their contacts, which is governed by the force-displacement law.
94 For dynamic calculations, the discrete element models follow an iterative, timestepping procedure
95 that consists of repeated update of particle positions and inter-particle forces at each timestep
96 (Cundall and Strack, 1999). This makes it possible to simulate the non-linear interaction of a series
97 of particles.

98

99 Due to the particle-based nature, the discrete element model can produce realistic faults and
100 fractures with a finite displacement. This method has been thereby widely used for modelling
101 structural deformations across a wide range of scales, especially for modelling development of
102 detachment fold (Hardy and Finch, 2005; Vidal-Royo et al., 2011; Meng and Hodgetts, 2019),
103 fault-bend fold (Benesh et al., 2007), fault-propagation fold (Finch et al., 2003, 2004; Cardozo et
104 al., 2005; Hardy and Finch, 2006, 2007; Hughes et al., 2014; Meng and Hodgetts, 2019) and
105 faults/fractures (e.g. Schöpfer et al., 2006, 2007, 2011, 2016, 2017; Abe et al., 2011; Hardy, 2013;
106 Spence and Finch, 2014; Virgo et al., 2013, 2014, 2016; Finch and Gawthorpe, 2017). The
107 extensive applications of discrete element modelling to structural geology research make it an ideal
108 method for addressing questions related to the present study.

109

110 **2.2. Model configuration**

111 Our discrete element models, constructed using the Particle Flow Code (Cundal and Strack, 1999),
112 consist of a 2 km long rectangular box that has a two vertical side walls, a basal floor and an open
113 top (Fig. 2b). The box is filled with numerous closely-packed, bonded particles with radii ranging

114 from 1.0 to 3.2 m, to represent overlying sediments in the overburden. A 0.2 km high, right-angled
115 equilateral triangle, located below the central part of the rectangular box, is filled with 18,516 non-
116 bonded particles with radii ranging from 0.5 to 1 m, to represent fluidized sands. Notably, the
117 geometry of the sandbody is highly simplified, and the aim of such a geometry is to allow the
118 particles within the sandbody to radially spread upwards. Particle sizes in both the sandbody and
119 the overburden follow a Gaussian distribution, which can help avoid hexagonal close packing of
120 particles.

121
122 The particle stiffness is assigned with a value of $1e7$ N/m for both normal (k_n) and shear (K_s)
123 stiffness, which are appropriate values for sandstones and correspond to a Young's Modulus of
124 approximately 5 MPa for the bulk rock mass (Liu and Konietzky, 2018). Friction coefficient μ of
125 particles in the overburden is assigned with a value of 0.25, whilst μ for particles in the sandbody
126 is set to zero. The particle density ρ is 2600 kg/m³. The bonding cohesion for particles in the
127 overburden is set to be between 1 to 8 MPa, to represent sediments with a relatively low to high
128 cohesion.

129
130 The packing of particles was achieved by allowing an assembly of randomly-generated particles
131 to settle to the bottom of the model under their own weight. The system was considered to have
132 reached static equilibrium when the mean unbalanced force within the particle assembly have
133 dropped to a negligible value. The particle assembly was then trimmed to the desired height, which
134 led to a small amount of vertical elastic rebound and elevated the surface. We then repeated the
135 trimming process that allowed the system to be settled. The particle assembly in the overburden
136 was trimmed to a height of 0.28, 0.35 and 0.42 km, to represent a relatively thin to thick overburden

137 respectively. The overburden sediments are mechanically homogeneous. Colours were assigned
138 to the overburden sediments simply for bedding correlations.

139

140 The model boundaries are defined by elastic walls that share the same mechanical properties with
141 their contacting particles. Deformation of the system was driven by a horizontal wall underneath
142 the sandbody that moved upward at a constant rate of 0.5 m per timestep. This helps represent a
143 lithostatic stress condition during sand fluidization and inflation. The models were gravitationally
144 loaded by 1 g.

145

146 We mainly focused on the macroscopic deformations and structures generated as a result of
147 sandbody inflation, especially on forced folds and faults/fractures. Only the models that exhibit
148 realistic features are presented. The models that reproduced classical, widely reported structures
149 were selected for a more detailed analysis, regarding their sequential deformation processes and
150 evolving stress fields. By varying the cohesion and thickness of particles in the overburden, we
151 also made an evaluation of their control on the development and patterns of inflation-related
152 structures.

153

154 **3. Results**

155 **3.1. Modelling results**

156 **3.1.1. Series 1: models 1-4**

157 Models 1-4 with a relatively thin overburden exhibited varied deformation patterns in the
158 overburden. Model 1 produced multiple normal faults in the layers above the sandbody (Fig. 3a).
159 Two faults (F1 and F2) propagated to the surface as through-going faults, and created fault scarps

160 in the uppermost layer during normal slipping. F1 and F3, which are dipping towards opposite
161 directions, constitute a small horst located above a symmetrical sand dome. F2 and F4 occur along
162 the margins of the sandbody, with the fault-bounded blocks acting as footwalls.

163

164 Model 2 produced multiple small normal blind faults in the sediments below the magenta layer
165 (Fig. 3b). These faults correspond to the concaves and convexes on the irregular sandbody surface.
166 Notably, a forced fold was formed in the overburden. An opening-mode fracture was generated in
167 the fold hinge, where the layers exhibit the maximum curvature. This fracture propagated
168 downwards to the magenta layer and exhibits a downward tapering tip.

169

170 Similar to model 2, model 3 produced a force fold and an opening-mode fracture that reached
171 downwards to the orange layer (Fig. 3c). Below the orange layer, a minor normal fault was
172 developed due to the cone-shaped sand intrusion that uplifted the sediments in the footwall. The
173 other parts of the forced fold are smoothly curved.

174

175 Model 4 produced a force fold in the overlying sediments of the sandbody, however, the
176 overburden remained intact with no faults being formed (Fig. 3d). The layers are smoothly curved
177 and parallel to the upper sandbody surface.

178

179 **3.1.2. Series 2: models 5-10**

180 The modelling result of model 5 is rather similar to that of model 1, regarding fault patterns and
181 sandbody surface geometry. Model 5 produced multiple normal faults that transect the sediments
182 above the sandbody (Fig. 4a), with fault scarps being created on the surface. A sand dome with a

183 rounded top protruded into the overlying sediments, with a through-going faults developed along
184 its right flank. Normal faults are also developed along the margins of the sandbody.

185

186 Model 6 produced two normal faults in the sediments above the sandbody, and a cone-shaped sand
187 protrusion with a sharp top (Fig. 4b). The two normal faults define a small horst above the sand
188 protrusion. One of the faults is a through-going fault developed along the flank of sand protrusion.

189 Two opening voids were created during fault slip due to the irregularities on the fault surface. The
190 sandbody exhibits an asymmetric geometry, and its surface remains largely planar.

191

192 Model 7 produced two minor blind normal faults that cut layers between the sandbody and the
193 magenta layer (Fig. 4c). These two faults define a minor horst that was formed due to the uplift of
194 the sediments by sand protrusion. Interestingly, a void was created between the gray layer and the
195 magenta layer, where the two faults intersect, due to strata collapse. The sandbody surface is
196 largely planar except the concave segment on the right of the fault that allowed accommodation of
197 the sediments in the hanging-wall.

198

199 A graben side-by-side with two horsts was formed in model 8, which is bounded by two minor
200 normal faults (Fig. 4d). Two opening voids were created where faults intersect, because of strata
201 collapse in the hangingwalls of the normal faults, similar to model 7. The sandbody surface
202 exhibits a concave, with two faults developed along its flanks. The concave accommodated
203 sediments in the graben.

204

205 Model 9 produced a normal fault that occurs along the left flank of a cone-shaped sand protrusion,
206 and reached the red layer (Fig. 4e). The fracture tip can be subdivided into a hybrid-mode, inclined
207 segment, and an opening-mode sub-vertical segment. Notably, the inclined segment is aligned
208 normal to the surface of the surface of the underlying sandbody.

209

210 Model 10 produced a rather symmetric forced fold in the overburden (Fig. 4f). Similar to model 4,
211 the layers and the sandbody surface were smoothly curved and parallel with each other. No faults
212 were formed in this model.

213

214 **3.1.3. Series 3: models 11-18**

215 Model 11 produced a large horst with normal faults developed along the margins of the sandbody
216 (Fig. 5a). The faults on the left of the sandbody are through-going faults, resulting in a fault scarp
217 on the surface. The sandbody surface is relatively planar comparing to the other models.

218

219 Similar to model 11, model 12 also produced a horst in the sediments above the sandbody (Fig.
220 5b). Differently, the fault F2 passed into a reverse fault above the blue layer, resulting in a push-
221 up structure on the surface. Two parallel opening-mode fractures were generated due to the normal
222 displacement of F1.

223

224 Model 13 produced two high-angle reverse faults in the overburden that resulted in a push-up
225 structure on the surface, with two fault scarps being created (Fig. 5c). The sandbody surface
226 exhibits a sub-rounded small dome in its center. The dome caused gentle folding of the beds below
227 the magenta layer, whilst the upper layers were not influenced.

228

229 Model 14 produced three main faults, including an opening-mode fracture (F1) in the hinge of the
230 forced fold, and a pair of oppositely dipping faults (F2 and F3) below the green layer (Fig. 5d).
231 Both F2 and F3 have a closed, lower segment with a reverse displacement, and an upper segment
232 occurring in an opening-mode. Interestingly, the opening, inclined segment of F2 passed into a
233 sub-horizontal, purely opening-mode fracture towards its tapering tip.

234

235 The modelling results of models 15 and 16 are similar (Fig. 5e, f). Both models produced a normal
236 fault F1 in the hinge of the forced fold with their upper segments occurring in a hybrid mode, and
237 a reverse fault F2 passing into an opening fracture. Similar to model 14, the opening segment of
238 F2 of model 16 also consist of a sub-horizontal, tapering tip that occurs in a pure opening mode.

239

240 Model 17 produced two main faults in the overburden, including one in the fold hinge and the
241 other as a hybrid fracture developed along the sandbody margin (Fig. 5g). Differently from
242 previous two models, F1 in the fold hinge exhibits a reverse displacement. Notably, the opening
243 segments of F2 consists of steep en echelon fractures and horizontal steps that link neighbouring
244 steep fractures.

245

246 Model 18 only generated one opening fracture, with a reverse sense of shear, in the hinge of the
247 force fold (Fig. 5h). The layers are smoothly curved, without additional fractures being produced
248 to cut the overburden.

249

250 **3.2. Syn-intrusion deformation and stress field in the overburden**

251 Two models (5 and 14) that appear to be the most compatible with natural observations of
252 sandstone intrusions regarding injectite geometry and fault/ fracture patterns, were selected for a
253 more detailed analysis of the entire intrusion process and syn-intrusion deformations in the
254 overburden.

255

256 **3.2.1. Model 5**

257 Model 5 produced an array of normal faults in the overburden, with distinguishable normal
258 displacement and fault scarps, and a rather symmetric dome on the sandbody surface (Figs 4a and
259 6). Initially (T1), the overburden remained intact whilst a small amount of sands were intruded
260 into the overlying layers (Fig. 4a). This led to concentration of horizontal tensile stresses in the
261 upper layers of the overburden (Fig. 4b). Later (T2), a minor dome was formed in the central part
262 of the sandbody, resulting in differential compactions of the upper gray and orange layers and the
263 subsequent formation of a minor blind normal fault. The stress field was dominated by
264 compressive stresses in the surrounding area of the injectites, whilst horizontal tensile stresses
265 were increasingly intensive in the uppermost layers of the overburden above the sandbody. At T3,
266 the dome continued to grow with an increasing dome height. The minor fault propagated upward
267 to the magenta layer. The stress field is similar to that at the earlier stages, only more intensified
268 of the tensile stresses in the upper layers. After that (T4), a through-going normal fault was formed
269 that transected the entire overburden, with an opening fault scarp being developed on the
270 overburden surface. Meanwhile, minor normal faults with oppositely-dipping directions were
271 generated at the sandbody margins. The extent of tensile stress distribution became narrower than
272 the previous stage. In particular, tensile stresses were dropped dramatically in the fault zones. At
273 T5, F2, that is parallel to F1, propagated to the overburden surface as a through-going fault. This

274 was accompanied with a decreased extent of the horizontal tensile stresses to be in the hangingwall
275 rocks of F2 right above the sandbody. At the final stage, both the width and height of the dome
276 increased, leading to increased fault displacement of all faults in the overburden. The system
277 exhibits a pattern similar to a half graben. The stress field is similar to that at T5.

278

279 **3.2.2. Model 14**

280 Model 14 produced a pair of oppositely-dipping, opening mode fractures in the overburden (Figs
281 5d and 7). Initially (T1), although the intrusion of the sandbody sands did not cause distinguishable
282 deformation in the overburden (Fig. 7a), it gave rise to the development of tensile stress
283 concentrations located in the upmost layers above the channel (Fig. 7b). At the following stage
284 (T2), the sandbody exhibited a domal surface, which is smoothly curved across the entire surface.
285 The tensile stresses became more intensified, and the stress trajectories were aligned in a half-
286 circular manner above the sandbody. At T3, a vertical opening-mode fracture was formed,
287 accompanied with a dramatic drop of tensile stress in the uppermost layers. Later (T4), a pair of
288 conical, opening-mode fractures were formed where tensile stresses were concentrated. Tensile
289 stresses were concentrated in the tip regions of the opening-mode fractures. At T5, the size of both
290 conical fractures increased significantly. The left fracture propagated upwards by the linkage of
291 several sub-parallel en echelon fractures and their sub-horizontal steps. The opening segments of
292 the conical fractures did not exhibit relative displacement of fracture walls, whilst the lower
293 segments of the fractures were closed and exhibited a reverse displacement. At the final stage (T6),
294 the left fracture, with a horizontal fracture tip, reached the red layer. Aperture of all the three
295 opening fractures were increased. The distribution of tensile stresses was similar to the previous

296 stages (T4 and T5), i.e. the tensile stresses were mainly localized within fracture tip regions and
297 adjacent areas.

298

299 **3.3. Surface deformation**

300 Most of the models presented produced forced folding of the overburden due to the intrusion of
301 sandbody sands, except model 5. Here, we focus on the forced folding of the surface layer,
302 regarding the fold amplitude and wavelength that are represented by the maximum surface uplift
303 and width of the uplifted domain respectively. Fig. 8 shows the plot of overburden rock cohesion
304 versus the maximum surface uplift and width of the uplifted domain, to reveal their relationships.
305 It is demonstrated that, in general, a higher cohesion of the overburden rocks can result in a greater
306 surface uplift, and a greater width as well, although exceptions occur. The greatest surface uplift
307 of 66.6 m occurs in model 10 that has the highest cohesion among model series 2. Model 18 that
308 has the highest cohesion among all models, exhibits the greatest width of an uplifted domain of
309 1.22 km.

310

311 **4. Discussion**

312 **4.1. Controls on forced folding of the overburden**

313 Intrusion-related, forced folds have been commonly found to develop above sandstone intrusions
314 with domal surfaces (Nichols, 1995; Frey-Martnez et al., 2007; Hamberg et al., 2007; Szarawarska
315 et al., 2010), in a manner analogous with forced folding induced by igneous intrusions (e.g. Hansen
316 and Cartwright, 2006; Hansen et al., 2008; Jackson et al., 2013; Omosanya et al., 2017). Forced
317 folding occurs in the sedimentary cover overlying remobilised sand bodies during their mechanical
318 emplacement, in order to compensate for the added thickness provided by the intruded sands

319 (Hansen et al., 2008). Forced folds are, thereby, regarded as a diagnostic feature of an intrusive
320 origin (Szarawarska et al., 2010). Forced folds are of great importance for both depositional and
321 structural analysis. Forced folds associated with sand intrusions may control the thickness and
322 stratal architecture of subsequently deposited units (Frey-Martnez et al., 2007; Huuse et al., 2007;
323 Cartwright et al., 2008). Moreover, onlap onto the flanks of forced folds allows dating of the
324 intrusions (Shoulders and Cartwright, 2004; Shoulders et al., 2007). Although forced folds that are
325 accompanied with sandstone intrusions have received increasing attention, the controls on the fold
326 geometries, aside from the volume of intruded sands, are difficult to be determined, due to the lack
327 of comparisons of forced folds developed in different geological contexts. A recent study has
328 suggested that, for igneous intrusions, the cohesion of sedimentary covers could control the
329 geometry of forced folds and the aspect ratios of intrusive bodies as revealed by sandbox
330 experiments (Schmiedel et al., 2017).

331

332 Here, our models can help address this issue by varying the value of one parameter whilst the
333 others being kept constant. It is demonstrated in the modelling results that both the cover rock
334 cohesion and overburden thickness are crucial controlling factors for forced folds (Fig. 8). The
335 cover rock cohesion exhibits a positive correlation to the size of forced fold, i.e. the higher the
336 cohesion is, the greater the fold amplitude and wavelength are. Forced fold may not be formed
337 during forceful injection of sands, if the intrusion timing is early and the cover sediments has a
338 very low cohesion, i.e. a low degree of lithification. With the same cover rock cohesion, the forced
339 folds predominantly exhibit a lower amplitude when the overburden is thicker. The relationship
340 between the wavelength of forced folds and fold amplitude is unclear for models with the same
341 cover rock cohesion, indicating that fold wavelength is more intimately associated with cover rock

342 cohesion, whilst overburden thickness may play a much less important role in controlling
343 wavelength of forced folds.

344

345 It should be noted that some other factors that were not considered in this study, can also influence
346 the geometry and size of forced folds, including stiffness of the cover sediments, variations of
347 mechanical properties across the sedimentary successions (i.e. mechanical stratigraphy), and
348 spatial variations of those factors.

349

350 **4.2. Faulting and fracturing mechanisms**

351 **4.2.1. Failure mode**

352 Generally, sandstone intrusions are regarded as opening-mode, natural hydraulic fractures that
353 occur when fluid pressure within remobilised sands exceeds the sum of the minimum principal
354 stress and tensile strength of the host rock (Cosgrove, 2001; Jolly and Lonergan, 2002; Cartwright
355 et al., 2008; Cartwright, 2010). Remobilised materials can then exploit these faults/fractures as
356 transport pathways due to the fact that they are the mechanically easier option (Weertman, 1980;
357 Donnadieu and Merle, 1998). However, the structural response of the flexed overburden during
358 the early stage of sand inflation, especially prior to overpressure, has been largely ignored.

359

360 The modelling results presented demonstrate that shear, tensile and hybrid fault/fractures (both
361 normal and reverse) can be induced in the overburden by inflation of sandbodies and forceful
362 intrusion of sands into the overlying sediments. These fault/fractures are predominantly fold-
363 related, due to differential compaction in the adjacent sediments during progressive fold
364 development, which largely agrees with Cosgrove and Hillier (1999).

365

366 The fold-related faults/fractures can be subdivided into three main types, including 1) normal (Figs
367 3a-b, 4a-e, 5a-b,) and reverse faults (Fig. 5b-g) that correspond to the irregularities of the sandbody
368 surface, and also along sandbody margins; 2) inclined or sub-horizontal pure tensile fractures
369 aligned along the channel margins, and are not directly connected to the sandbody (Fig. 5d-g); and
370 3) pure tensile, or hybrid subvertical, downward propagating fractures in the hinge zones of the
371 forced fold (Figs 3b-c, 5d-h).

372

373 Faults/fractures of type I can be attributed to differential compaction induced by the intrusive
374 bodies, and their formation mechanism is further discussed in the following section.
375 Faults/fractures of type II have been commonly observed in seismic data as dyke-sill complexes,
376 and are referred to as winglike structures (Huuse et al., 2007; Jackson et al., 2007; Jackson et al.,
377 2011; Jackson and Sømme, 2011). Fault/fractures of type III have been reported to be associated
378 with intrusions (Cosgrove and Hillier, 1999; Hansen and Cartwright, 2006; Mathieu et al., 2008),
379 as the result of curvature-related stretching and subsequent tensile fracturing in the hinge zones of
380 intrusion-induced force folds. It is, therefore, believed that the three series of models have
381 successfully reproduced many characteristic features of sandstone intrusion-related folds and
382 faults/fractures.

383

384 **4.2.2. Intrusion-induced normal faults vs. pre-existing polygonal faults**

385 It has been recognised that normal faulting can be triggered by sandstone intrusions as a result of
386 gravitational collapse off sand domes (Dixon et al., 1995; Palladino, et al., 2018). The intrusion-
387 related normal faults have been suggested to have dramatically modified the geometries of the

388 depositional sand bodies, and influenced formation and propagation of sand dykes and sill
389 complexes in the Late Paleocene and Early Eocene submarine sandstone reservoirs in the Bruce-
390 Beryl Embayment, northern North Sea (Dixon et al., 1995), Eocene Alba Field, UKCS (Cosgrove
391 and Hiller, 2000) and also in central California (Palladino, et al., 2018). Our models with a low
392 cover rock cohesion and a thin to intermediate overburden thickness, i.e. models 1, 5 and 6, largely
393 agree to this explanation. Moreover, our models well illustrate the relationship between the
394 development of sand domes and nucleation and propagation of normal faults (Fig. 6).

395
396 Polygonal faults (Fig. 9), occurring as networks of early diagenetically induced shear failure of
397 fine-grained sediments (Cartwright, 1994, 2011; Cartwright and Lonergan, 1996; Gouly, 2008;
398 Davies et al., 2009), have been frequently found to coexist with sandstone intrusions in the North
399 Sea (Huuse et al., 2004; Huuse and Mickelson, 2004; Jackson et al., 2007, 2011; Shoulders et al.,
400 2007; Szarawarska et al., 2010). It has been suggested that the pre-existing normal faults may have
401 facilitated sandstone remobilisations and injections along dilated polygonal fault planes (Lonergan
402 and Cartwright, 1999; Molyneux et al., 2002). However, some intrusions have been observed not
403 to be affected by polygonal faults (Bureau et al., 2013). Moreover, the normal faults were found
404 to be predominantly steeper than polygonal faults (Shoulders et al., 2007), indicating that not all
405 the normal faults within sand intrusion-bearing layers can be simply interpreted as pre-existing
406 polygonal faults.

407
408 Our modelling results help verify that normal faults can be formed as a result of sandstone intrusion
409 (Figs 3a-b, 4a-e, 5a-b), due to differential compaction in the overlying sediments caused by sand
410 doming, especially when the sediment cohesion is low, i.e. the timing of sand intrusion is early.

411 This can help explain the origin of some normal faults developed in the sediments overlying the
412 sandbody. It is likely that many normal faults could result from differential compaction during the
413 development of irregular sandbody surfaces as they intrude upwards. The sediments on the
414 footwalls may experience more uplift by sand domes (or mounds), causing relative motions of
415 sediments on different sides of the domes and subsequent normal faulting. Notably, due to the
416 early timing of intrusion, the overlying sediments were not fully consolidated, allowing a localized
417 intrusion-related compaction of those sediments, without causing a volumetric expansion. Hence,
418 surface uplift or significant forced folding would not occur under such conditions (Figs 3a and 4a).

419

420 **4.2.3. Dyke-sill complex**

421 It has been reported that sandstone intrusions commonly consist of inclined dykes and
422 subhorizontal sills (Jackson et al., 2011). Dykes are commonly observed to be aligned along
423 sandbody margins and were described as winglike structures (Huuse et al., 2004; Jackson et al.,
424 2011). Sills serve either as frontmost tips of injectites passed from upward propagating dykes, or
425 as steps that link adjacent dykes (Lonergan et al., 2000; Jackson et al., 2011). Models 14-17 well
426 reproduced fault/fracture systems that resemble the dyke-sill complexes described in previous
427 studies.

428

429 The winglike dykes developed along margins of remobilised channels have been suggested to
430 occur as peripheral dykes (Cosgrove and Hillier, 1999) due to different strains within a flexed
431 overburden above intrusive bodies (Pollard and Johnson, 1973). However, our modelling results
432 suggests that differential compaction would lead to nucleation and upward propagation of reverse
433 faults along sandbody margins rather than pure opening-mode, upward-tapering fractures (Fig. 5d-

434 g). The reverse faults passed into opening-mode fractures as they propagated upwards, either in a
435 hybrid mode or in a pure tensile mode. The reverse sense of shear becomes neglectable in the tips
436 of those opening-mode fractures (Fig. 5f).

437

438 Models 14 and 17 demonstrate the development of sub-horizontal sills that link neighbouring
439 dykes. Those sills were generated as dilational jogs in the tip overlapping zones of dykes during
440 their propagation, which is evident from both field (Jolly and Lonergan, 2002) and seismic
441 observations (Jackson et al., 2011). Alternative explanations of sills in dyke-sill complexes were
442 attributed to local stress variations or pre-existing mechanical weaknesses, such as bedding
443 (Pollard and Johnson, 1973; Boehm and Moore, 2002; Kavanagh et al., 2006; Cartwright et al.,
444 2008; Menand, 2008) or unconformity (Huuse et al., 2004). However, our models 14, 16 and 17
445 produced sub-horizontal opening fractures as the frontmost tip of the intrusion-induced fractures
446 in a homogenous media (Fig. 5). Such fractures can serve as preferential sites for subsequent
447 storage of remobilised sands, and evolve into sills. It is, therefore, argued that the formation of sub-
448 horizontal sills, especially the frontmost segments of winglike structures, may not result from
449 either local stress variations, or mechanical heterogeneities, such as bedding. Instead, they may be
450 produced by tensile stresses originated as a result of the uplift of the overlying sediments of
451 remobilised sands. Notably, this can only be possible when the sediments have a cohesion high
452 enough to prevent gravitational collapse and fracture healing.

453

454 **4.3. Implications for the storage of injected sands**

455 Due to the complexity of sand injectites and the insufficient seismic resolution in mapping steeply
456 dipping sand units, it can be problematic to characterise the geometry, size and distribution of

457 subsurface sand injectites, especially the sub-seismic injectites (Jackson et al., 2007). Nevertheless,
458 our modelling results provide new insights for predicting preferential sites for the storage of sand
459 injectites. Such sites mainly include: 1) opening voids created along irregular surfaces of intrusion-
460 induced faults during fault slip (Fig. 4b); 2) opening spaces created on top of grabens due to strata
461 collapse (Fig. 4c-e); and 3) middle-upper segments of conical fractures that are aligned along
462 sandbody margins (Fig. 5d-g). These sites provide opening spaces that can preferentially
463 accommodate fluidised sands when the sands enter these sites and fluid pressure is dropped to be
464 insufficient to jack up shear fractures.

465
466 It is possible that the winglike dykes may not emanate from sandbody margins as previous
467 suggested, due to the prevalent compressive stresses that dominant the areas adjacent to the
468 remobilised sands (Fig. 7b). The reverse faults that are attached to the sandbody can be dilated and
469 serve as transport pathways for fluidized sands, however, they may be closed when fluid pressure
470 drops, and thereby not favour sand storage. Differently, the intrusion-related fractures may occur
471 in an opening mode in their middle to upper segments, and can accommodate injected sands that
472 migrate along the fractures and enter these parts. Fig. 10 shows a field example of remobilised
473 sands with a steeply-dipping wing sheet in the Triassic marls of the Mercia Mudstone Group,
474 Somerset, SW England, which can help verify the point made above. The wing sheet exhibits clear
475 thickness variations along its propagation direction. The lower segment of the wing exhibits a
476 downward tapering tip, and is not directly connected to the sub-horizontal basal sandbody in the
477 2D section. The wing sheet shares the same grain size and mineral composition with the basal
478 sandbody, and has been suggested to be sand injectites sourced from the basal sandbody during its
479 remobilisation (Meng et al., 2017). The geometry of this sand wing and the spatial relationships

480 between the wing and its source sandbody demonstrate that sand wings resulted from sand
481 remobilisations may not in all cases directly emanate from sandbody margins, and that the faulted
482 areas adjacent to remobilised sands may not be consistently open throughout the entire sand
483 remobilisation and favour sand storage.

484

485 It is worth mentioning that the models presented are highly simplified, without aiming to directly
486 simulate any specific natural prototypes. The main limitations of our models are that the roles of
487 fluid pressure, mechanical stratigraphy and sandbody geometry were not considered. It is,
488 therefore, suggested that future studies can incorporate these factors, especially for specific case
489 studies with regional and local geological contexts being provided.

490

491 **5. Conclusions**

492 This study utilized the discrete element modelling method to simulate overburden forced folding
493 and fracturing induced by inflation of fluidised sandbodies. We conclude the following:

494 (1) Inflation of fluidised sands can trigger normal faulting of the overburden when the host
495 sediments have a low cohesion, i.e. a low level of lithification. The formation of normal faults can
496 be attributed to sand doming-induced differential compaction in the overlying sediments.

497

498 (2) Sandstone inflation can result in forced folding of the overlying, cemented sediments and
499 thereby a flexed overburden. Differential compaction across the inflated sandbody can produce
500 faults/fractures along channel margins and also in fold hinge zones.

501

502 (3) The modelling results demonstrate a positive correlation between the cohesion of the overlying
503 sediments and the amplitude and wavelength of the forced fold, i.e. the higher the cohesion is, the
504 greater the amplitude and wavelength of the force fold are. With the same cover rock cohesion,
505 the forced fold will exhibit a lower amplitude if the overburden is thicker. The overburden
506 thickness does not play an important role in controlling the wavelength of the forced fold.

507

508 (4) The differential compaction induced by sandstone inflation can result in conical, opening
509 fractures that consist of both steep and subhorizontal segments. The formation of sub-horizontal
510 opening fractures may not necessarily be attributed to local stress variations or mechanical
511 heterogeneities in the overburden, but could result from tensile stresses developed due to uplift of
512 the overlying sediments above remobilised channels. Such fractures could evolve into dyke-sill
513 complexes when fluidized sands entered these fractures.

514

515 (5) Our modelling results suggest that opening spaces that favour the storage of remobilised sands
516 mainly include 1) voids created along faults with irregular, rough fault planes; 2) opening spaces
517 created above intrusion-induced grabens; and 3) middle-upper opening segments of conical
518 faults/fractures that are aligned along channel margins.

519

520 **Acknowledgements**

521 This work was supported by the Sandstone Injection Research Group (SIRG) consortium. Itasca
522 is thanked for technical support. We thank Mads Huuse and Andrew Hurst for beneficial
523 suggestions.

524

525 **References**

- 526 Abe, S., Van Gent, H., Urai, J.L., 2011. DEM simulation of normal faults in cohesive materials.
527 Tectonophysics 512, 12-21.
- 528 Benesh, N.P., Plesch, A., Shaw, J.H., Frost, E.K., 2007. Investigation of growth fault bend folding
529 using discrete element modeling: Implications for signatures of active folding above blind
530 thrust faults. Journal of Geophysical Research: Solid Earth 112, B03S04,
531 doi:10.1029/2006JB004466.
- 532 Boehm, A., Moore, J.C., 2002. Fluidized sandstone intrusions as an indicator of paleostress
533 orientation, Santa Cruz, California. Geofluids 2, 147-161.
- 534 Bureau, D., Mourgues, R., Cartwright, J., 2014. Use of a new artificial cohesive material for
535 physical modelling: Application to sandstone intrusions and associated fracture networks.
536 Journal of Structural Geology 66, 223-236.
- 537 Bureau, D., Mourgues, R., Cartwright, J., Foschi, M., Abdelmalak, M.M., 2013. Characterisation
538 of interactions between a pre-existing polygonal fault system and sandstone intrusions
539 and the determination of paleo-stresses in the Faroe-Shetland basin. Journal of Structural
540 Geology 46, 186-199.
- 541 Cardozo, N., Allmendinger, R.W., Morgan, J.K., 2005. Influence of mechanical stratigraphy and
542 initial stress state on the formation of two fault propagation folds. Journal of Structural
543 Geology 27, 1954-1972.
- 544 Cartwright, J.A., 1994. Episodic basin-wide fluid expulsion from geopressed shale sequences in
545 the North Sea basin. Geology 22, 447-450.

- 546 Cartwright, J.A., Lonergan, L., 1996. Volumetric contraction during the compaction of mudrocks:
547 a mechanism for the development of regional-scale polygonal fault systems. *Basin*
548 *Research* 8, 183-193.
- 549 Cartwright, J., Huuse, M., 2005. 3D seismic technology: the geological 'Hubble'. *Basin Research*
550 17, 1-20.
- 551 Cartwright, J., 2007. The impact of 3D seismic data on the understanding of compaction, fluid
552 flow and diagenesis in sedimentary basins. *Journal of the Geological Society* 164, 881-
553 893.
- 554 Cartwright, J., Huuse, M., Aplin, A., 2007. Seal bypass systems. *AAPG Bulletin* 91, 1141-1166.
- 555 Cartwright, J., James, D., Huuse, M., Vetel, W., Hurst, A., 2008. The geometry and emplacement
556 of conical sandstone intrusions. *Journal of Structural Geology* 30, 854-867.
- 557 Cartwright, J., 2010. Regionally extensive emplacement of sandstone intrusions: a brief review.
558 *Basin Research* 22, 502-516.
- 559 Cartwright, J., 2011. Diagenetically induced shear failure of fine-grained sediments and the
560 development of polygonal fault systems. *Marine and Petroleum Geology* 28, 1593-1610.
- 561 Cosgrove, J.W., Hillier, R.D., 1999. Forced-fold development within Tertiary sediments of the
562 Alba Field, UKCS: evidence of differential compaction and post-depositional sandstone
563 remobilization. *Geological Society, London, Special Publications* 169, 61-71.
- 564 Cosgrove, J.W., 2001. Hydraulic fracturing during the formation and deformation of a basin: A
565 factor in the dewatering of low-permeability sediments. *AAPG Bulletin* 85, 737-748.
- 566 Cundall, P.A., Strack, O.D.L., 1979. A discrete numerical model for granular assemblies.
567 *Geotechnique* 29, 47-65.

- 568 Cundall, P.A., Strack, O.D.L., 1999. Particle flow code in 2 dimensions. Itasca consulting group,
569 Inc.
- 570 Davies, R.J., Huuse, M., Hirst, P., Cartwright, J., Yang, Y., 2006. Giant clastic intrusions primed
571 by silica diagenesis. *Geology* 34, 917-920.
- 572 Davies, R.J., Ireland, M.T., Cartwright, J.A., 2009. Differential compaction due to the irregular
573 topology of a diagenetic reaction boundary: a new mechanism for the formation of
574 polygonal faults. *Basin Research* 21, 354-359.
- 575 de Boer, W., Rawlinson, P.B., Hurst, A., 2007. Successful exploration of a sand injectite complex:
576 Hamsun prospect, Norway Block 24/9. *AAPG Memoir* 87, 65-68.
- 577 Diller, J.S., 1890. Sandstone dikes. *Bulletin of the Geological Society of America* 1, 411-442.
- 578 Dixon, R.J., Schofield, K., Anderton, R., Reynolds, A.D., Alexander, R.W.S., Williams, M.C.,
579 Davies, K.G., 1995. Sandstone diapirism and clastic intrusion in the Tertiary submarine
580 fans of the Bruce-Beryl Embayment, Quadrant 9, UKCS. Geological Society, London,
581 Special Publications 94, 77-94.
- 582 Donnadieu, F., Merle, O., 1998. Experiments on the indentation process during cryptodome
583 intrusions: New insights into Mount St. Helens deformation. *Geology* 26, 79-82.
- 584 Finch, E., Hardy, S., Gawthorpe, R., 2003. Discrete element modelling of contractional fault-
585 propagation folding above rigid basement fault blocks. *Journal of Structural Geology* 25,
586 515-528.
- 587 Finch, E., Hardy, S., Gawthorpe, R., 2004. Discrete-element modelling of extensional fault-
588 propagation folding above rigid basement fault blocks. *Basin Research* 16, 467-488.

- 589 Finch, E., Gawthorpe, R., 2017. Growth and interaction of normal faults and fault network
590 evolution in rifts: insights from three-dimensional discrete element modelling. Geological
591 Society, London, Special Publications 439, <https://doi.org/10.1144/SP439.23>.
- 592 Frey-Martnez, J., Cartwright, J., Hall, B., Huuse, M., 2007. Clastic intrusion at the base of deep-
593 water sands: A trap-forming mechanism in the eastern Mediterranean. AAPG Memoir 87,
594 49-63.
- 595 Goult, N.R., 2008. Geomechanics of polygonal fault systems: a review. Petroleum Geoscience
596 14, 389-397.
- 597 Hamberg, L., Jepsen, A.M., Ter Borch, N., Dam, G., Engkilde, M.K., Svendsen, J.B., 2007.
598 Mounded structures of injected sandstones in deep-marine Paleocene reservoirs, Cecilie
599 field, Denmark. AAPG Memoir 87, 69-79.
- 600 Hansen, D.M., Cartwright, J., 2006. The three-dimensional geometry and growth of forced folds
601 above saucer-shaped igneous sills. Journal of Structural Geology 28, 1520-1535.
- 602 Hansen, D.M., Redfern, J., Federici, F., Di Biase, D., Bertozzi, G., 2008. Miocene igneous activity
603 in the Northern Subbasin, offshore Senegal, NW Africa. Marine and Petroleum Geology
604 25, 1-15.
- 605 Hardy, S., Finch, E., 2005. Discrete-element modelling of detachment folding. Basin Research 17,
606 507-520.
- 607 Hardy, S., Finch, E., 2006. Discrete element modelling of the influence of cover strength on
608 basement-involved fault-propagation folding. Tectonophysics 415, 225-238.
- 609 Hardy, S., Finch, E., 2007. Mechanical stratigraphy and the transition from trishear to kink-band
610 fault-propagation fold forms above blind basement thrust faults: a discrete-element study.
611 Marine and Petroleum Geology 24, 75-90.

- 612 Hardy, S., 2013. Propagation of blind normal faults to the surface in basaltic sequences: Insights
613 from 2D discrete element modelling. *Marine and Petroleum Geology* 48, 149-159.
- 614 Haug, Ø., Galland, O., Souloumiac, P., Souche, A., Guldstrand, F., Schmiedel, T., Maillot, B.,
615 2018. Shear Versus Tensile Failure Mechanisms Induced by Sill Intrusions: Implications
616 for Emplacement of Conical and Saucer-Shaped Intrusions. *Journal of Geophysical*
617 *Research: Solid Earth* 123, 3430-3449.
- 618 Hubbard, S.M., Romans, B.W., Graham, S.A., 2007. An outcrop example of large-scale
619 conglomeratic intrusions sourced from deep-water channel deposits, Cerro Toro
620 Formation, Magallanes basin, southern Chile. *AAPG Memoir* 87, 199-207.
- 621 Hughes, A.N., Benesh, N.P., Shaw, J.H., 2014. Factors that control the development of fault-bend
622 versus fault-propagation folds: Insights from mechanical models based on the discrete
623 element method (DEM). *Journal of Structural Geology* 68, 121-141.
- 624 Hurst, A., Cartwright, J., Duranti, D., 2003a. Fluidization structures produced by upward injection
625 of sand through a sealing lithology. Geological Society, London, Special Publications 216,
626 123-138.
- 627 Hurst, A., Cartwright, J., Huuse, M., Jonk, R., Schwab, A., Duranti, D., Cronin, B., 2003b.
628 Significance of large-scale sand injectites as long-term fluid conduits: evidence from
629 seismic data. *Geofluids* 3, 263-274.
- 630 Hurst, A., Cartwright, J.A., Huuse, M., Duranti, D., 2006. Extrusive sandstones (extrudites): A
631 new class of stratigraphic trap? Geological Society, London, Special Publications 254,
632 289-300.
- 633 Hurst, A., Cartwright, J., 2007. Relevance of sand injectites to hydrocarbon exploration and
634 production. *AAPG Memoir* 87, 1-19.

- 635 Hurst, A., Scott, A., Vigorito, M., 2011. Physical characteristics of sand injectites. *Earth-Science*
636 *Reviews* 106, 215-246.
- 637 Hurst, A., Huuse, M., Duranti, D., Vigorito, M., Jameson, E., Schwab, A., 2016. Application of
638 outcrop analogues in successful exploration of a sand injection complex, Volund Field,
639 Norwegian North Sea. Geological Society, London, Special Publications 436, 75-92.
- 640 Hurst, A., Vigorito, M., 2017. Saucer-shaped sandstone intrusions: An underplayed reservoir
641 target. *AAPG Bulletin* 101, 625-633.
- 642 Huuse, M., Duranti, D., Guargena, C.G., Prat, P., Holm, K., Steinsland, N., Cronin, B.T., Hurst,
643 N., 2003. Sandstone intrusions: Detection and significance for exploration and production.
644 *First Break* 21, 15-24.
- 645 Huuse, M., Duranti, D., Steinsland, N., Guargena, C.G., Prat, P., Holm, K., Cartwright, J.A., Hurst,
646 A., 2004. Seismic characteristics of large-scale sandstone intrusions in the Paleogene of
647 the south Viking Graben, UK and Norwegian North Sea. Geological Society, London,
648 *Memoirs* 29, 263-278.
- 649 Huuse, M., Mickelson, M., 2004. Eocene sandstone intrusions in the Tampen Spur area
650 (Norwegian North Sea Quad 34) imaged by 3D seismic data. *Marine and Petroleum*
651 *Geology* 21, 141-155.
- 652 Huuse, M., Shoulders, S.J., Netoff, D.I., Cartwright, J., 2005a. Giant sandstone pipes record basin-
653 scale liquefaction of buried dune sands in the Middle Jurassic of SE Utah. *Terra Nova* 17,
654 80-85.
- 655 Huuse, M., Cartwright, J.A., Gras, R., Hurst, A., 2005b. Kilometre-scale sandstone intrusions in
656 the Eocene of the Outer Moray Firth (UK North Sea): migration paths, reservoirs and

- 657 potential drilling hazards. *Petroleum Geology: North-West Europe and Global*
658 *Perspectives—Proceedings of the 6th Petroleum Geology Conference, 1577–1594.*
- 659 Huuse, M., Cartwright, J., Hurst, A., Steinsland, N., 2007. Seismic characterization of large-scale
660 sandstone intrusions. *Geological Society, London, Memoirs, 29, 263-278.*
- 661 Huuse, M., Jackson, C.A.L., Van Rensbergen, P., Davies, R.J., Flemings, P.B., Dixon, R.J., 2010.
662 *Subsurface sediment remobilization and fluid flow in sedimentary basins: an overview.*
663 *Basin Research 22, 342-360.*
- 664 Itasca, 2004. *Particle Flow Code in 2-Dimensions (PFC2D) manual version 3.10.* Minneapolis,
665 Minnesota.
- 666 Jackson, C.A.L., Hurst, A., Cartwright, J.A., 2007. The geometry, distribution and development
667 of clastic injectites in deep-marine depositional systems: Examples from the Late
668 Cretaceous Kyrre Formation, Måløy slope, Norwegian margin. *Sand injectites:*
669 *Implications for hydrocarbon exploration and production: AAPG Memoir 87, 37-48.*
- 670 Jackson, C.A.L., Huuse, M., Barber, G.P., 2011. Geometry of winglike clastic intrusions adjacent
671 to a deep-water channel complex: Implications for hydrocarbon exploration and
672 production. *AAPG Bulletin 95, 559-584.*
- 673 Jackson, C.A.L., Sømme, T.O., 2011. Borehole evidence for wing-like clastic intrusion complexes
674 on the western Norwegian margin. *Journal of the Geological Society 168, 1075-1078.*
- 675 Jackson, C.A.L., Schofield, N., Golenkov, B., 2013. Geometry and controls on the development
676 of igneous sill-related forced folds: A 2-D seismic reflection case study from offshore
677 southern Australia. *Geological Society of America Bulletin 125, 1874-1890.*
- 678 Jenkins, O.P., 1930. Sandstone dikes as conduits for oil migration through shales. *AAPG Bulletin*
679 *14, 411-421.*

- 680 Jolly, R.J.H., Lonergan, L., 2002. Mechanisms and controls on the formation of sand intrusions.
681 Journal of the Geological Society 159, 605-617.
- 682 Kavanagh, J.L., Menand, T., Sparks, R.S.J., 2006. An experimental investigation of sill formation
683 and propagation in layered elastic media. Earth and Planetary Science Letters 245, 799-
684 813.
- 685 Liu, Y., Konietzky, H., 2018. Particle-based modelling of pull-apart basin development. Tectonics
686 37, 343-358.
- 687 Løseth, H., Raulline, B., Nygård, A., 2013. Late Cenozoic geological evolution of the northern
688 North Sea: development of a Miocene unconformity reshaped by large-scale Pleistocene
689 sand intrusion. Journal of the Geological Society 170, 133-145.
- 690 Lonergan, L., Cartwright, J.A., 1999. Polygonal faults and their influence on deep-water sandstone
691 reservoir geometries, Alba Field, United Kingdom central North Sea. AAPG Bulletin 83,
692 410-432.
- 693 Lonergan, L., Lee, N., Johnson, H.D., Cartwright, J.A., Jolly, R.J.H., 2000. Remobilisation and
694 injection in deepwater depositional systems: Implications for reservoir architecture and
695 prediction. GCSSEPM Foundation 20th Annual Research Conference: Deep-Water
696 Reservoirs of the World, 515-532.
- 697 Lonergan, L., Borlandelli, C., Taylor, A., Quine, M., Flanagan, K., 2007. The three-dimensional
698 geometry of sandstone injection complexes in the Gryphon field, United Kingdom North
699 Sea. AAPG Memoir 87, 103-112.
- 700 Mathieu, L., De Vries, B.V.W., Holohan, E.P., Troll, V.R., 2008. Dykes, cups, saucers and sills:
701 Analogue experiments on magma intrusion into brittle rocks. Earth and Planetary Science
702 Letters 271, 1-13.

- 703 Menand, T., 2008. The mechanics and dynamics of sills in layered elastic rocks and their
704 implications for the growth of laccoliths and other igneous complexes. *Earth and*
705 *Planetary Science Letters* 267, 93-99.
- 706 Meng, Q., Hooker, J., Cartwright, J., 2017. Genesis of natural hydraulic fractures as an indicator
707 of basin inversion. *Journal of Structural Geology* 102, 1-20.
- 708 Meng, Q., Hodgetts, D., 2019. Combined control of décollement layer thickness and cover rock
709 cohesion on structural styles and evolution of fold belts: A discrete element modelling
710 study. *Tectonophysics*, <https://doi.org/10.1016/j.tecto.2019.03.004>.
- 711 Molyneux, S., Cartwright, J.A., Lonergan, L., 2002. Conical amplitude anomalies as evidence for
712 large scale sediment intrusions. *First Break* 20, 123-129.
- 713 Moreau, J., Ghienne, J.F., Hurst, A., 2012. Kilometre-scale sand injectites in the intracratonic
714 Murzuq Basin (South-west Libya): an igneous trigger? *Sedimentology* 59, 1321-1344.
- 715 Mourgues, R., Bureau, D., Bodet, L., Gay, A., Gressier, J.B., 2012. Formation of conical fractures
716 in sedimentary basins: Experiments involving pore fluids and implications for sandstone
717 intrusion mechanisms. *Earth and Planetary Science Letters* 313, 67-78.
- 718 Nichols, R.J., 1995. The liquification and remobilization of sandy sediments. Geological Society,
719 London, Special Publications 94, 63-76.
- 720 Omosanya, K.O., Johansen, S.E., Eruteya, O.E., Waldmann, N., 2017. Forced folding and complex
721 overburden deformation associated with magmatic intrusion in the Vøring Basin, offshore
722 Norway. *Tectonophysics* 706, 14-34.
- 723 Palladino, G., Grippa, A., Bureau, D., Alsop, G.I., Hurst, A., 2016. Emplacement of sandstone
724 intrusions during contractional tectonics. *Journal of Structural Geology* 89, 230-249.

- 725 Palladino, G., Alsop, G.I., Grippa, A., Zvirtes, G., Phillip, R.P., Hurst, A., 2018. Sandstone-filled
726 normal faults: A case study from central California. *Journal of Structural Geology*, 110,
727 86-101.
- 728 Peterson, G.L., 1966. Structural interpretation of sandstone dikes, northwest Sacramento Valley,
729 California. *Geological Society of America Bulletin* 77, 833-842.
- 730 Pollard, D.D., Johnson, A.M., 1973. Mechanics of growth of some laccolithic intrusions in the
731 Henry Mountains, Utah, II: bending and failure of overburden layers and sill formation.
732 *Tectonophysics* 18, 311-354.
- 733 Rodrigues, N., Cobbold, P.R., Løseth, H., 2009. Physical modelling of sand injectites.
734 *Tectonophysics* 474, 610-632.
- 735 Schöpfer, M.P.J., Childs, C., Walsh, J.J., 2006. Localisation of normal faults in multilayer
736 sequences. *Journal of Structural Geology* 28, 816-833.
- 737 Schöpfer, M.P.J., Childs, C., Walsh, J.J., 2007. Two-dimensional distinct element modeling of the
738 structure and growth of normal faults in multilayer sequences: 1. Model calibration,
739 boundary conditions, and selected results. *Journal of Geophysical Research: Solid Earth*
740 112, B10401, doi:10.1029/2006JB00490.
- 741 Schöpfer, M.P.J., Arslan, A., Walsh, J.J., Childs, C., 2011. Reconciliation of contrasting theories
742 for fracture spacing in layered rocks. *Journal of Structural Geology* 33, 551-565.
- 743 Schöpfer, M.P.J., Childs, C., Walsh, J.J., Manzocchi, T., 2016. Evolution of the internal structure
744 of fault zones in three-dimensional numerical models of normal faults. *Tectonophysics*
745 666, 158-163.

- 746 Schöpfer, M.P.J., Childs, C., Manzocchi, T., Walsh, J.J., 2017. Three-dimensional distinct element
747 method modelling of the growth of normal faults in layered sequences. Geological
748 Society, London, Special Publications 439, 307-332.
- 749 Schmiedel, T., Galland, O., Breitzkreuz, C., 2017. Dynamics of sill and laccolith emplacement in
750 the brittle crust: Role of host rock strength and deformation mode. Journal of Geophysical
751 Research: Solid Earth 122, 8860-8871.
- 752 Scott, A., Hurst, A., Vigorito, M., 2013. Outcrop-based reservoir characterization of a kilometer-
753 scale sand-injectite complex. AAPG Bulletin 97, 309-343.
- 754 Shoulders, S.J., Cartwright, J., 2004. Constraining the depth and timing of large-scale conical
755 sandstone intrusions. Geology 32, 661-664.
- 756 Shoulders, S.J., Cartwright, J., Huuse, M., 2007. Large-scale conical sandstone intrusions and
757 polygonal fault systems in Tranche 6, Faroe-Shetland Basin. Marine and Petroleum
758 Geology 24, 173-188.
- 759 Spence, G.H., Finch, E., 2014. Influences of nodular chert rhythmites on natural fracture networks
760 in carbonates: an outcrop and two-dimensional discrete element modelling study.
761 Geological Society, London, Special Publications 374, SP374-318.
- 762 Szarawarska, E., Huuse, M., Hurst, A., De Boer, W., Lu, L., Molyneux, S., Rawlinson, P., 2010.
763 Three-dimensional seismic characterisation of large-scale sandstone intrusions in the
764 lower Palaeogene of the North Sea: completely injected vs. in situ remobilised sandbodies.
765 Basin Research 22, 517-532.
- 766 Vétel, W., Cartwright, J., 2010. Emplacement mechanics of sandstone intrusions: insights from
767 the Panoche Giant Injection Complex, California. Basin Research 22, 783-807.

- 768 Vidal-Royo, O., Hardy, S., Muñoz, J.A., 2011. The roles of complex mechanical stratigraphy and
769 syn-kinematic sedimentation in fold development: insights from discrete-element
770 modelling and application to the Pico del Águila anticline (External Sierras, Southern
771 Pyrenees). Geological Society, London, Special Publications 349, 45-60.
- 772 Vigorito, M., Hurst, A., Cartwright, J., Scott, A., 2008. Regional-scale subsurface sand
773 remobilization: geometry and architecture. Journal of the Geological Society 165, 609-
774 612.
- 775 Virgo, S., Abe, S., Urai, J.L., 2013. Extension fracture propagation in rocks with veins: Insight
776 into the crack-seal process using Discrete Element Method modeling. Journal of
777 Geophysical Research: Solid Earth 118, 5236-5251.
- 778 Virgo, S., Abe, S., Urai, J.L., 2014. The evolution of crack seal vein and fracture networks in an
779 evolving stress field: Insights from Discrete Element Models of fracture sealing. Journal
780 of Geophysical Research: Solid Earth 119, 8708-8727.
- 781 Virgo, S., Abe, S., Urai, J.L., 2016. The influence of loading conditions on fracture initiation,
782 propagation, and interaction in rocks with veins: Results from a comparative Discrete
783 Element Method study. Journal of Geophysical Research: Solid Earth 121, 1730-1738.
- 784 Weertman, J., 1980. The stopping of a rising, liquid-filled crack in the Earth's crust by a freely
785 slipping horizontal joint. Journal of Geophysical Research: Solid Earth 85, 967-976.

786

787 **Figure captions**

788 Fig. 1. Schematic diagrams illustrating the changed channel geometries after sand remobilisation.

789 Note the domal or irregular surface of remobilised channels. Modified from (Lonergan et al., 2000).

790

791 Fig. 2. (a) Geometry and boundary conditions of the discrete element models. The enlarged area
792 shows particle contacts. (b) Two particles bounded by a normal and shear spring.

793

794 Fig. 3. Modelling results of models 1-4 with a relatively thin overburden. The bonding cohesion
795 increases from 1 to 4 MPa from model 1 to 4. Dashed lines represent fault traces. Arrows indicate
796 relative displacement.

797

798 Fig. 4. Modelling results of models 5-10 with an intermediate-thickness overburden. The bonding
799 cohesion increases from 1 to 6 MPa from model 5 to 10. The enlarged boxes show detailed features
800 of opening voids and fractures. Dashed lines represent fault traces. Arrows indicate relative
801 displacement.

802

803 Fig. 5. Modelling results of models 11-18 with a relatively thick overburden. The bonding cohesion
804 increases from 1 to 8 MPa from model 11 to 18. The enlarged boxes show detailed features of
805 opening voids and fractures. Dashed lines represent fault traces. Arrows indicate relative
806 displacement.

807

808 Fig. 6. Evolving deformation patterns (a) and stress fields (b) of model 5 during incremental sand
809 injections. A number of 463, 1221, 2281, 3571, 5087 and 6863 particles were injected into the
810 overlying layers at T1 to T6.

811

812 Fig. 7. Evolving deformation patterns (a) and stress fields (b) of model 14 during incremental sand
813 injections. A number of 276, 1060, 2214, 3633, 5091 and 6751 particles were injected into the
814 overlying layers at T1 to T6.

815

816 Fig. 8. Plot of cove rock cohesion versus structural relief of the surface 'h' versus width of uplifted
817 area 'w' of the 18 discrete element models. See the illustration of measurement of h and w in Fig.
818 3d.

819

820 Fig. 9. Seismic profiles showing characteristics of remobilised channel sands and normal fault
821 systems developed in the overlying sediments. Note that the upper marker horizons were not
822 uplifted. (a) Five normal faults developed in sediments above a channel with an irregular surface.
823 Modified from (Jackson, 2007). Note the domes that uplifted the sediments on the footwall of F2.
824 (b) Three normal faults developed above a remobilised channel. Modified from (Jackson et al.,
825 2011). Note that faulting did not occur in the outer zones of the overlying sediments.

826

827 Fig. 10. Field photography and its line drawing showing remobilised channel sands in the Triassic
828 red marls of the Merica Mudstone Group, Somerset, UK. Note the inclined sand wing with a
829 downward tapering tip.

830

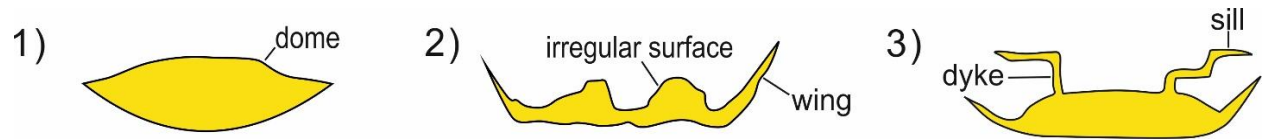


Fig. 1

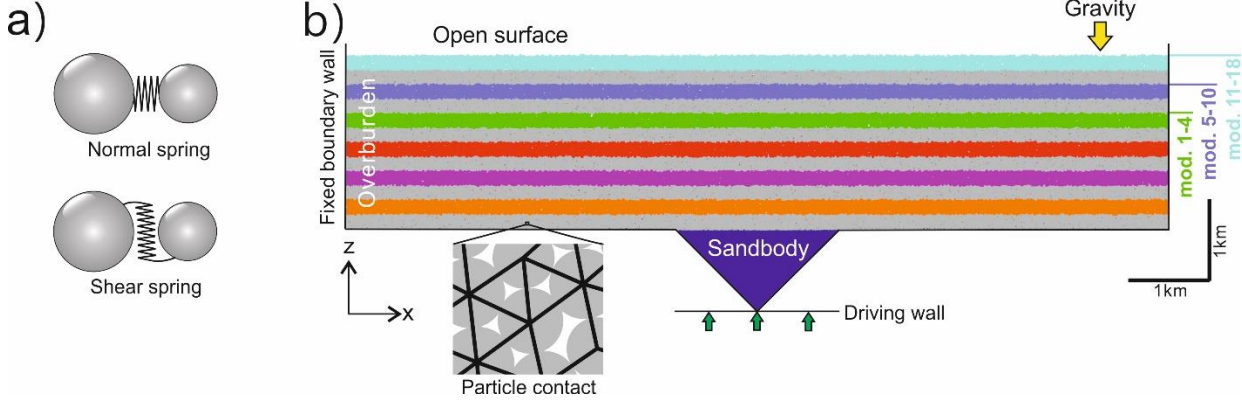


Fig. 2

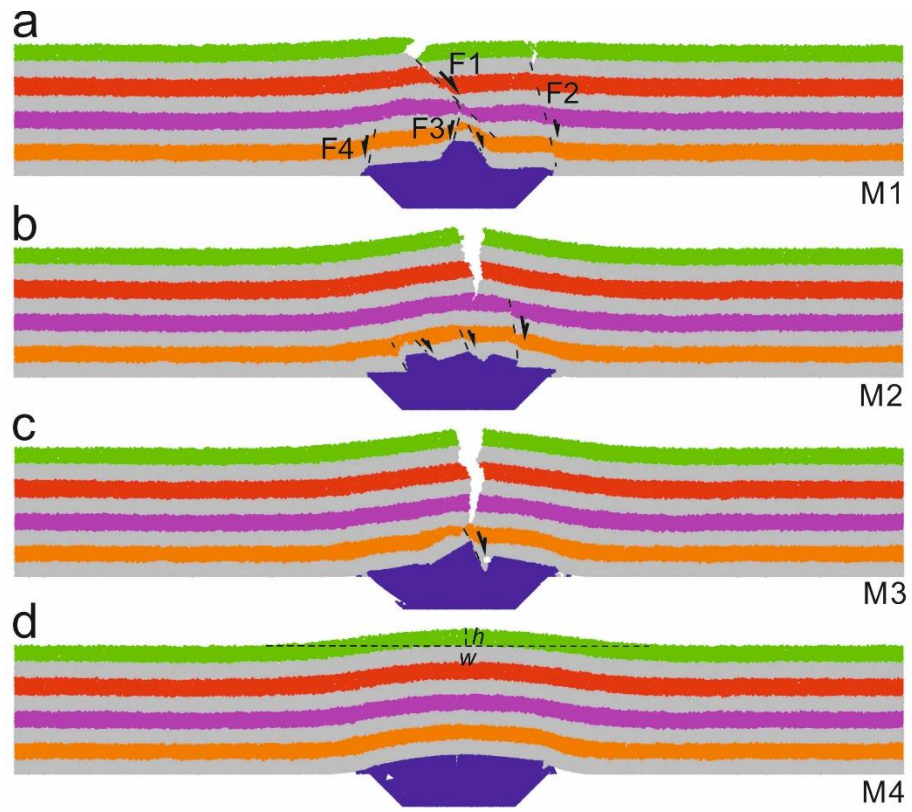


Fig. 3

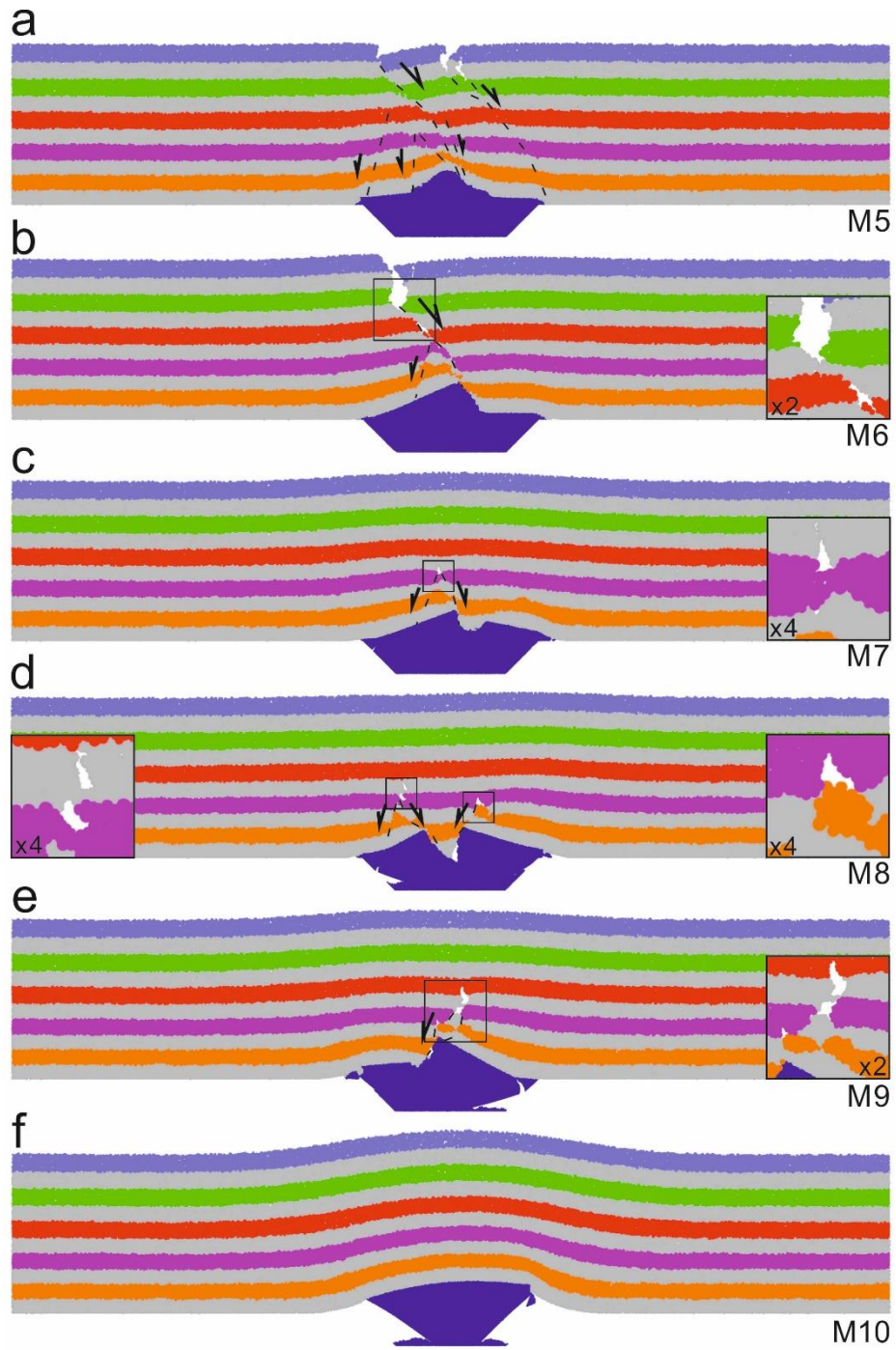


Fig. 4

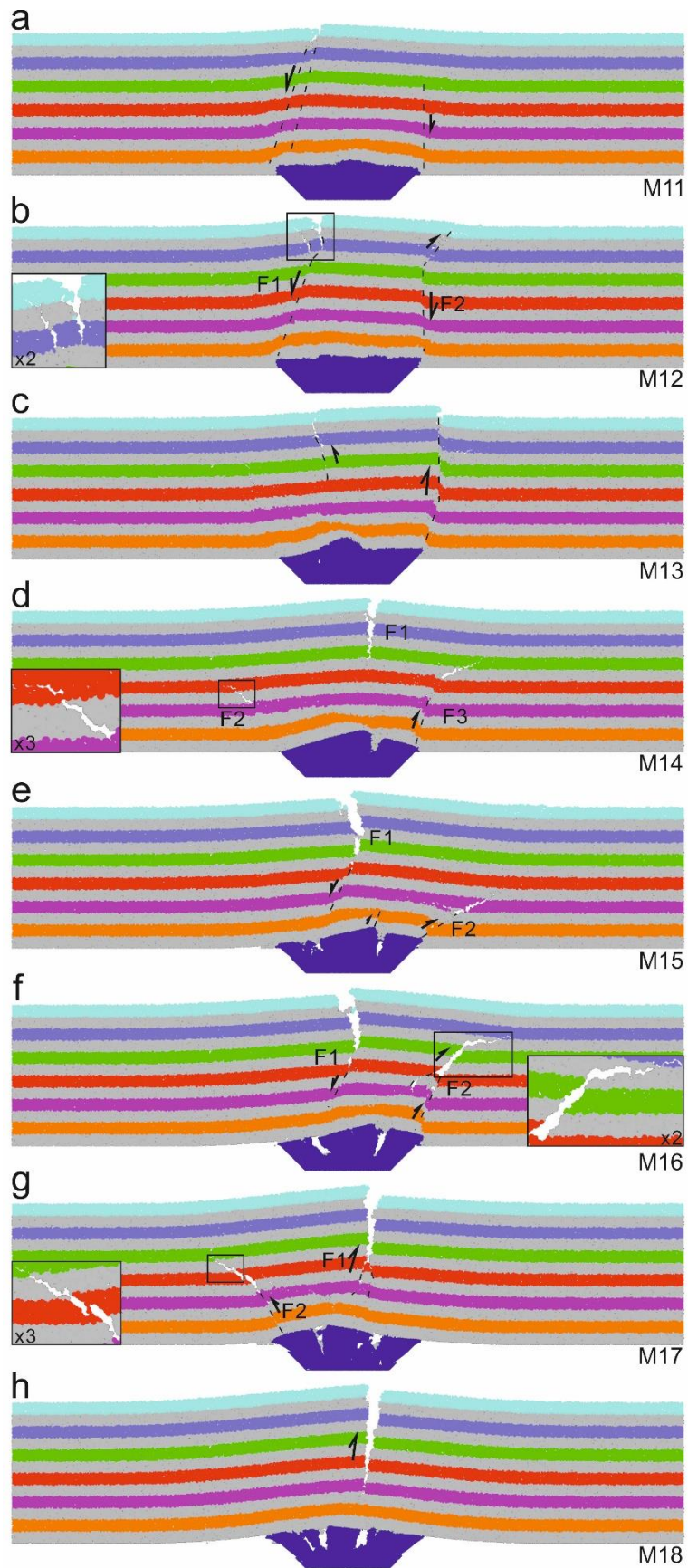


Fig. 5

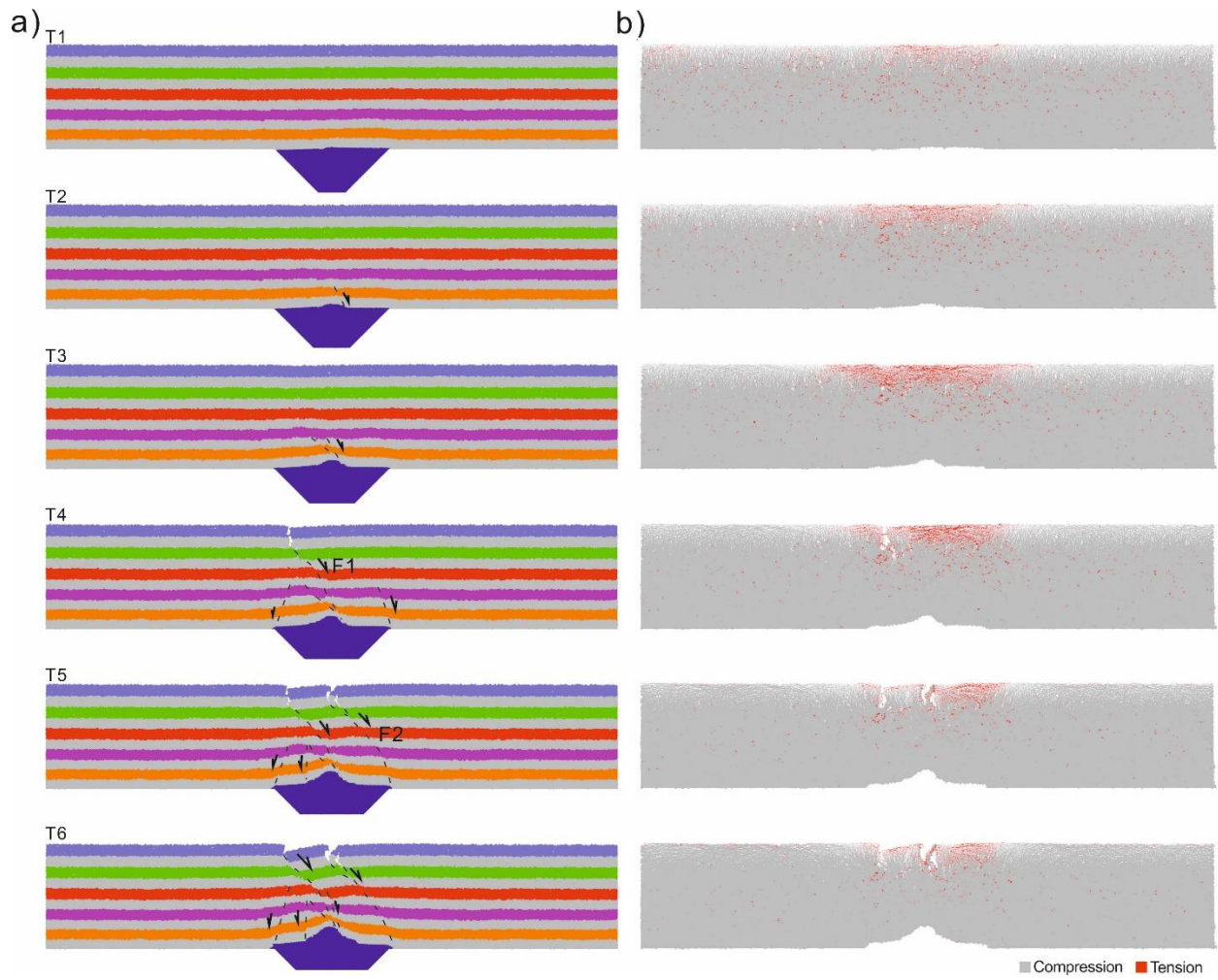


Fig. 6

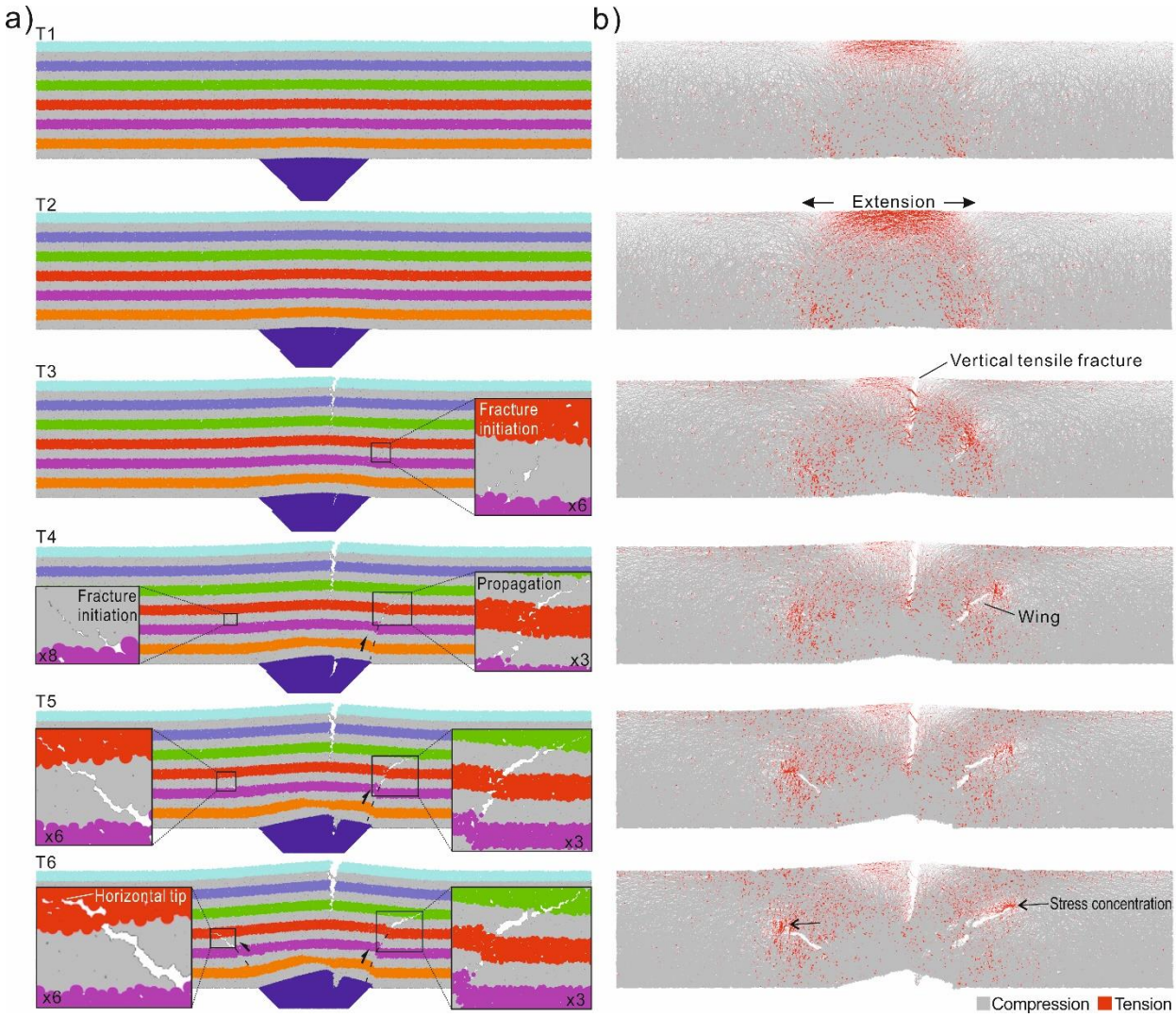


Fig. 7

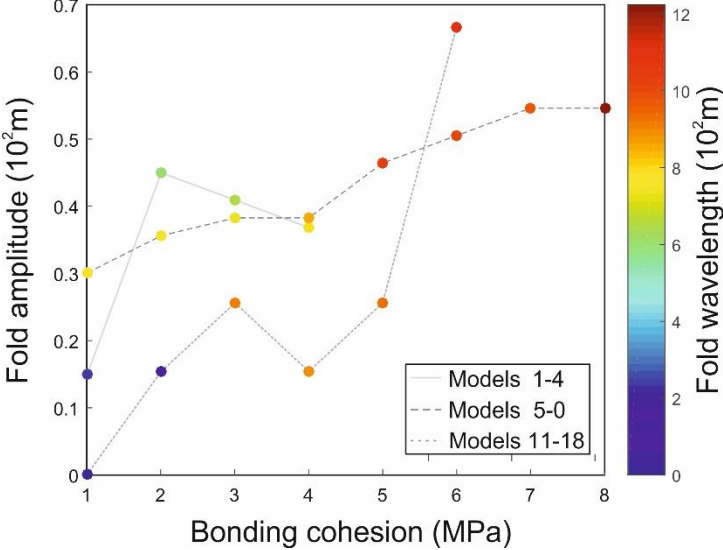


Fig. 8

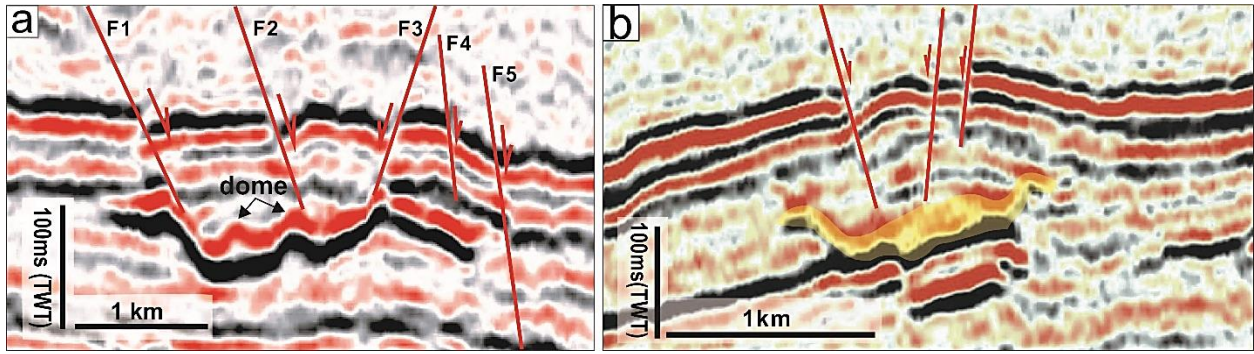


Fig. 9

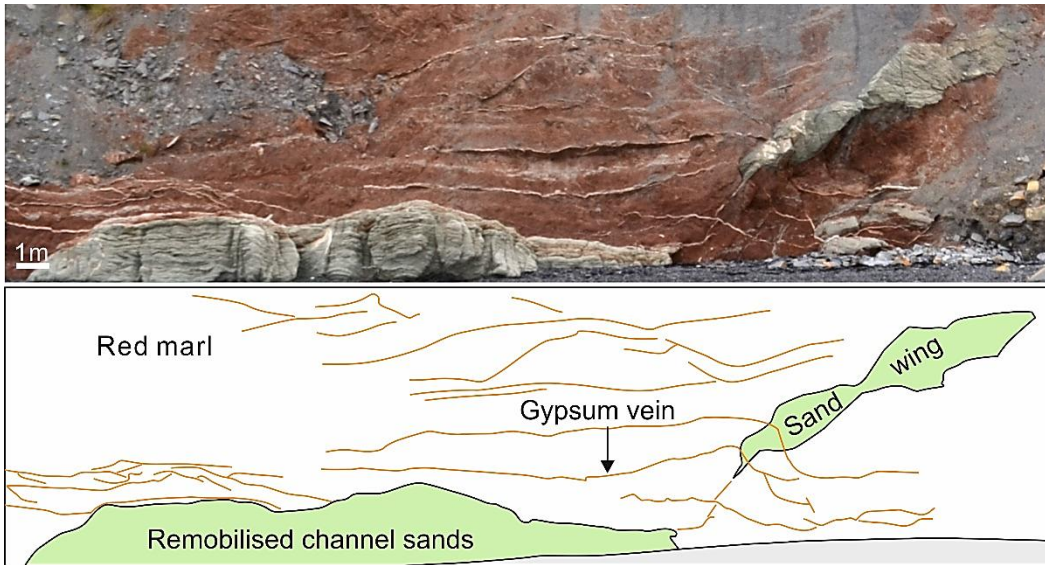


Fig. 10